

Neural network based time-resolved state tomography of superconducting qubits

Ziyang You,¹ Jiheng Duan,² Wenhui Huang,^{3,4} Libo Zhang,^{3,4} Song Liu,^{3,4} Youpeng Zhong,^{3,4} and Hou Ian^{1,*}

¹*Institute of Applied Physics and Materials Engineering, University of Macau, Macau, China*

²*Department of Physics and Astronomy, University of Rochester, Rochester, New York 14627, USA*

³*Shenzhen Institute for Quantum Science and Engineering,*

Southern University of Science and Technology, Shenzhen, China

⁴*International Quantum Academy, Shenzhen 518048, China*

Superconducting qubits have emerged as a premier platform for large-scale quantum computation, yet the fidelity of state readout is often hindered by random noise and crosstalk, especially in multi-qubit systems. While neural networks trained on labeled data have shown promise in reducing crosstalk effects during readout, their current capabilities are limited to binary discrimination of joint-qubit states due to architectural constraints. Here we introduce a time-resolved modulated neural network capable of full-state tomography for individual qubits, enabling detailed time-resolved measurements like Rabi oscillations. This scalable approach, with a dedicated module per qubit, mitigated readout error by an order of magnitude under low signal-to-noise ratios and substantially reduced variance in Rabi oscillation measurements. This advancement bolsters quantum state discrimination with neural networks, and propels the development of next-generation quantum processors with enhanced performance and scalability.

I. INTRODUCTION

Artificial intelligence (AI) has been increasingly utilized to address challenges across various domains of physics, including the field of quantum information science. The integration of AI with quantum physics, initially explored in molecular electronics [1], has expanded to include AI-assisted measurements in various quantum systems, including quantum light [2, 3], trapped ions [4, 5], and superconducting qubits [6–8]. Among these quantum systems, superconducting qubits have recently emerged as a leading platform for scalable quantum computation, offering remarkable coherence, controllability, and scalability [9–11]. These properties have paved the way for high-fidelity single and two-qubit gates, aligning with the requirements for surface-code quantum error correction [12]. However, the readout fidelity of superconducting qubits, particularly in simultaneous multi-qubit readouts, remains a significant hurdle [13–15]. In the context of circuit quantum electrodynamics, qubit states are typically inferred by detecting the state-dependent frequency shift in a coupled resonator [16–18]. This measurement process is vulnerable to various noise sources, such as $1/f$ noise [19, 20], flux noise [21], crosstalk [22, 23], and the qubit’s relaxation time [24, 25].

To address these challenges, machine learning techniques have been increasingly adopted [26, 27], offering a non-invasive approach to enhance quantum measurement fidelity without necessitating physical modifications to the quantum system [28, 29]. Neural networks, in particular, have demonstrated their efficacy in extracting meaningful features from raw data, bypassing the need for detailed error knowledge or reliance on pre-defined functions [28, 29]. For superconducting qubits,

neural networks have been employed to improve the fidelity of state discrimination between the ground and excited states [30–32]. They have also shown promise in analyzing joint states of multiple qubits. However, as the number of qubits increases, so does the complexity of the neural networks and the computational resources required. To date, neural networks have not been applied to perform complete qubit state tomography over extended periods, a task that requires a more sophisticated network architecture.

In this Letter, we introduce a time-resolved modulated neural network (TRMNN) specifically designed for the readout of single qubits in arbitrary superposition states. The TRMNN adopts a modular architecture, with each module featuring a fixed neural network, allowing for straightforward scalability by assigning one module per qubit. This design is optimized for continuous monitoring of the readout resonator, enabling comprehensive state tomography over user-defined durations, and facilitating the observation of Rabi oscillations at specific time intervals.

The TRMNN is built upon a feedforward neural network (FNN) and undergoes supervised learning using demodulated waveforms of dispersive readout when the qubit is in superposition of the ground and the excited states, see Fig. 1. The network is modulated in the sense that each qubit in the system is paired with an identical network module which is trained from data tagged either as the ground or the excited waveform samples. Compared to raw readout demodulated in the phase space, the post-processing neural network further enhances the readout fidelity through learned recognition of the pure signals from the noises in the measurements. The neural network essentially acquires node weights from reference waveforms associated with ground and excited qubit states through tagged data. A similarity score is subsequently generated through a linear output activation function by comparing each sampled waveform of un-

* houian@um.edu.mo

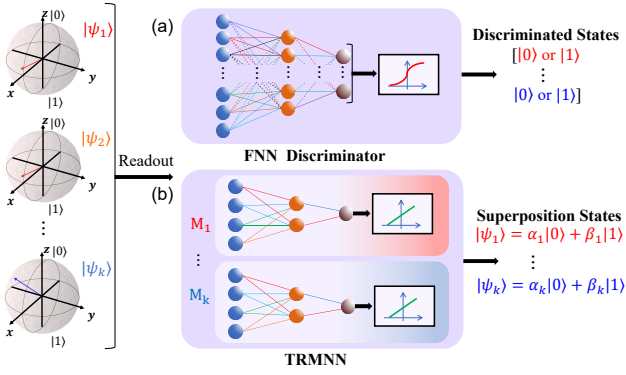


Figure 1. (a) The neural network architecture of the feed-forward neural network (FNN) discriminator comprises a complex neural network designed for discriminating between ground and excited states in multi-qubit systems. The blue, orange, and brown circles represent the input, hidden, and output layers, respectively. The softmax function is applied in the output layer, depicted by a red line as a nonlinear activation function. The softmax function acts as a binary classifier to enhance discrimination between the two states. (b) TRMNN consists of multiple modular neural networks (M_k). Each modular network is paired with a single qubit. A probability estimation function in the output layer is represented by a green line, indicating a linear activation function, and allowing for the measurement of arbitrary superpositions.

known states to the reference waveforms.

II. EXPERIMENTS AND RESULTS

We benchmark our neural network architecture with a single Xmon qubit coupled to a readout resonator in a lattice of six superconducting qubits [33], where the parameters of the testing qubit system are provided in Tab. III. The state information of the Xmon qubit is measured by probing a coupling resonator in the dispersive limit. The Hamiltonian of the qubit-resonator system is simplified as [34]

$$H_{\text{disp}}/\hbar = (\omega_r + \chi\sigma_z) \left(a^\dagger a + \frac{1}{2} \right) + (\omega_q + \chi) \frac{\sigma_z}{2}, \quad (1)$$

where ω_r denotes the bare frequency of the resonator, ω_q the qubit frequency, and $\chi = g^2/\Delta$ the state-dependent frequency shift due to the coupling strength g and the detuning $\Delta = \omega_r - \omega_q$ between the qubit and the resonator. Here, a change in the qubit state leads to an associated shift in the resonator frequency through the term $\chi\sigma_z$, which can be observed and quantified via a microwave probe signal [34]. In the experimental setup illustrated in Fig. 2, the probing signal is shaped by an arbitrary waveform generator (AWG) before reaching the target quantum chip. The response of the probing signal is successively amplified by a high electron-mobility transistor (HEMT) amplifier in low-temperature and a room-temperature low-noise amplifier. The qubit state

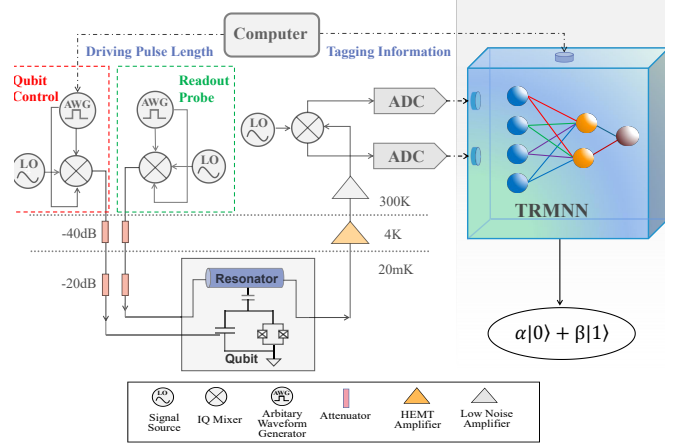


Figure 2. The system diagram illustrates the readout setup for a time-resolved modulated neural network (TRMNN). Qubit control and readout probe pulses are generated by arbitrary waveform generators (AWGs), upconverted by IQ mixers, and directed to the testing qubit through attenuators. The transmitted readout signal undergoes amplification, first by a high electron-mobility transistor (HEMT) amplifier at a 4K stage and then by a low-noise amplifier at room temperature. The TRMNN is implemented after the analog-to-digital converters (ADCs) to analyze the IQ-demodulated signal. A computer is utilized to send control commands to the AWG and provide tagging information for the corresponding waveform to the TRMNN during both the training and testing procedures.

is encoded in both the phase and the amplitude of the output probe signal. Considering a random noise term $N(t)$, the readout signal can be written as

$$S(t) = S_0 \cos(\omega_{\text{RO}}t + \theta_{\text{RO}}) + N(t), \quad (2)$$

where S_0 and θ_{RO} are the state-dependent amplitude and phase, respectively. The amplitude and phase are detected through a heterodyne measurement using an analog In-phase and Quadrature (IQ) mixer, which combines the readout signal $S(t)$ with a reference local oscillator (LO) along two branches.

Subsequently, the demodulated signals are sampled into a discrete-time sequence by analog-to-digital converters (ADCs) in the I and Q branches along with the noise. Each IQ pair measured is mapped to a specific point in the phase space as shown in Fig. 3, where two distinct clouds appear after a sufficient number of measurements. While the separation between the clouds reflects signal strength, the extension of each cloud shows the noise level $N(t)$. Subplots (a) and (c) illustrate two typical detection scenarios: one with low probe power (-134 dBm) and one with high probe power (-131 dBm). Along with the increase in probe power, the signal-to-noise ratio (SNR) is increased and thus the readout fidelity is enhanced from 80.1% to 97.3%.

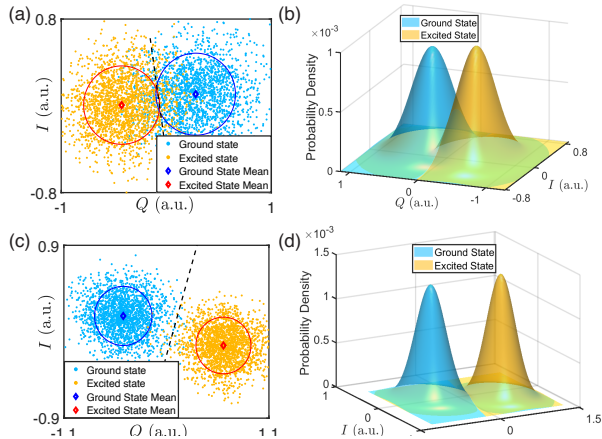


Figure 3. (a) The raw readout data are plotted in the phase space when the qubit is prepared in the ground and excited states in a low signal-to-noise ratio (SNR) case, with 2000 shots per qubit state (fidelity $F = 80.1\%$). The circles in red and blue represent the variances for each state. (b) Probability density regarded as Gaussian distributions with means and variances extracted from (a) for both ground and excited states. (c) The readout of the two states is plotted on the IQ plane in a high SNR case, with 2000 shots per qubit state (fidelity $F = 97.3\%$). (d) Same as (b) but with means and variances extracted from (c).

The noise effect embodied by the variance in the sampled data is persistent in both low and high SNR scenarios. To mitigate this, neural network methods have been widely adopted for recognizing categorized patterns and distilling features from data containing noise [35, 36]. We design the Time-Resolved Modulated Neural Network (TRMNN) to further process the sampled raw data such that the readout fidelity can be further increased, given the presence of noise.

Experimental assessments of qubit readout fidelity are conducted under both low and high SNR conditions in different readout settings. The readout performances of the raw readout, the FNN discriminator, and TRMNN are presented to provide a comprehensive evaluation. In the experiment, the dataset for each SNR setting comprises two subsets of 5000 single-shot waveforms for the ground and excited states, respectively. Within these subsets, 4000 sequences are allocated for training both the FNN discriminator and TRMNN, while the remaining 1000 sequences are reserved for testing.

The first evaluation of readout performance is the assignment fidelity [37], given by $F = 1 - [P(g|e) + P(e|g)]/2$. In this equation, $P(g|e)$ ($P(e|g)$) represents the probability of reading out the ground (excited) state when the qubit is prepared in the excited (ground) state. The assignment fidelity results for the three approaches are presented in Tab. I. In both high and low SNR cases, the fidelities of the FNN discriminator and the TRMNN exhibit improvements compared to the raw

F	High SNR	Low SNR
Raw Readout	97.3%	80.1%
FNN Discriminator	99.9%	98.6%
TRMNN	99.9%	98.5%

Table I. The assignment fidelities for the raw readout, the FNN discriminator, and TRMNN in the high and low SNR cases.

readout. For example, in the high SNR scenario, the two neural network-based approaches show a similar improvement in fidelity, increasing from 97.3% in the raw readout case to 99.9%. In the low SNR scenario, the fidelities of the FNN discriminator and the TRMNN experience a notable improvement from 80.1% to 98.5%, more than an order of magnitude improvement in terms of infidelity reduction. In the measurement of assignment fidelity, TRMNN consistently achieves similar performance to the FNN discriminator, even without a binary classifier like the softmax function in the neural network architecture.

The second evaluation is based on Rabi oscillation measurements to compare the readout performance when the qubit is in an arbitrary superposition state. Each Rabi oscillation measurement in the testing dataset comprises 40 samples taken at a fixed time step within a 200 ns interval, and the testing dataset includes 600 Rabi oscillation measurements. Similar to the previous experiment, two distinct datasets for both low and high SNR cases are recorded and analyzed by the trained neural networks to observe their performances in different scenarios. The measured oscillations of the excited state population with the Gaussian variance are presented in Figs. 4 and 5, where the curves represent averages of sequences with 10, 50, 100, and 600 Rabi oscillation measurements (M represents the number of measurements), respectively.

In Figs. 4 and 5, the results of the FNN Discriminator exhibit oscillations in trapezoid shapes, distinguishing them from the raw readout and TRMNN cases. This phenomenon arises from errors introduced by the softmax function in the output layer of the network. The softmax function tends to misclassify superposition states around the ground and excited states as purely ground or excited states, leading to enlargement around the peak and bottom of the curve. This misclassification is also evident in the increased variance in the FNN Discriminator curve around the region of the ground and excited states.

The raw readout and TRMNN display similar results of Rabi oscillations in both low and high SNR scenarios, making it challenging for a direct evaluation based on the shapes of curves. However, concerning the state variances, TRMNN shows a 48% reduction from the raw readout (1 to 0.52 and 0.15 to 0.078 a.u.) in the low and high SNR scenarios. The reduction in variance suggests that neural network-based approaches effectively reduce the impact of noise, aligning with the observed enhancement in assignment fidelity.

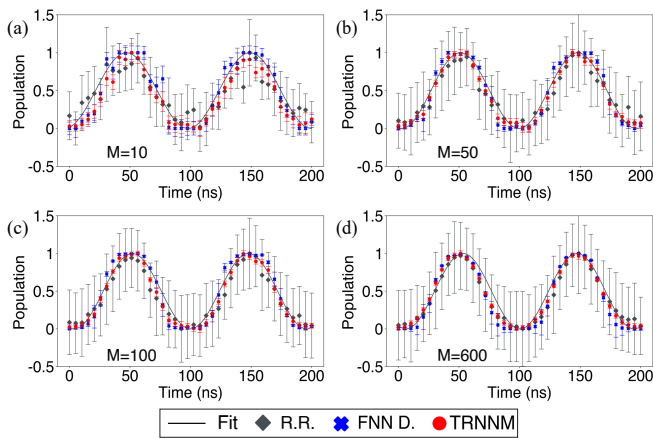


Figure 4. Measurements of the excited state population for low SNR (fidelity $F = 80.1\%$ at raw readout) over the duration of two Rabi oscillations using raw readout (gray diamonds), FNN discriminator (blue crosses), and TRMNN (red circles). Locations of the symbols indicate the statistical average of (a) $M = 10$, (b) $M = 50$, (c) $M = 100$, and (d) $M = 600$ measurement counts at each time step over 200 ns, where the error bar shows the Gaussian variance of the measurements. Under $M = 600$, the variances averaged over the entire time range are 1, 0.51, and 0.52 (a.u.) for the raw readout, the FNN discriminator, and TRMNN, respectively.

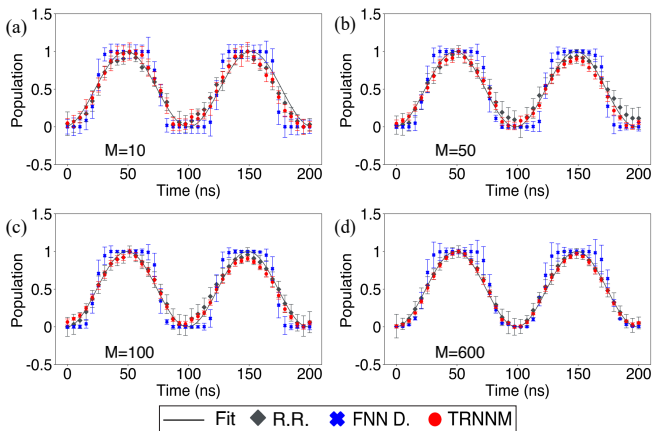


Figure 5. Identical measurements as in Fig. 4 except for high SNR (fidelity $F=97.3\%$ at raw readout). The temporally averaged variances are reduced to 0.15, 0.12, and 0.078 (a.u.) for the raw readout, the FNN discriminator, and TRMNN, respectively.

Another evaluation for the Rabi oscillation measurement involves fitting a sine function to the output curve and assessing the fitness since ideal Rabi oscillations have a sine wave pattern with a decaying envelope due to decoherence effects. Therefore, the fitness of a sine function within a short time period can evaluate the accuracy of the readout of Rabi oscillations, where the decoherence effect is not obvious. Here a Rabi fidelity is defined as F_R , derived from the calculation of the coefficient of determination [38] applied to the sine function fit as

F_R	M=10	M=50	M=100	M=600
Raw Readout (Low SNR)	0.849	0.928	0.947	0.955
FNN Discriminator (Low SNR)	0.951	0.966	0.968	0.960
TRMNN (Low SNR)	0.955	0.979	0.980	0.982
Raw Readout (High SNR)	0.959	0.986	0.989	0.996
FNN Discriminator (High SNR)	0.921	0.936	0.933	0.943
TRMNN (High SNR)	0.984	0.985	0.986	0.993

Table II. The Rabi fidelities by fitting the readout waveform with a sine function for the raw readout, the FNN discriminator, and the TRMNN, in a high and low SNR cases by averaging sequences of 10, 50, 100, and 600 times of Rabi oscillations measurement.

$$F_R = 1 - \sum_{i=1}^n \frac{(y_i - f_i)^2}{(y_i - \bar{y})^2}, \quad (3)$$

where y_i represents the measured value, f_i is the value from the fit at each sampling point, respectively, and \bar{y} is the average value of the measured curve. When the measured curve perfectly aligns with the sine function fit, the value of F_R equals unity.

Tab. II provides a summary of the F_R values of the three approaches in the two SNR cases with different numbers of averaged shots. In the low SNR case, TRMNN consistently exhibits the highest Rabi fidelity, irrespective of the number of averaged shots. This outcome reinforces the earlier observation that TRMNN effectively mitigates the adverse effects of noise and enhances overall readout fidelity compared to the raw readout. Meanwhile, the FNN Discriminator has the second-highest F_R value, which is consistent with the trapezoid shape error introduced by the softmax function. In the high SNR case, the results indicate that raw readout and TRMNN consistently obtain well-fitting sine outputs in high SNR scenarios. Nevertheless, TRMNN attains the highest result with a small number of measurements ($M = 10$), highlighting its potential application in single-shot readouts for state tomography.

III. CONCLUSION

In this study, we introduce a time-resolved modulated neural network specifically designed for high-fidelity qubit state tomography. This approach effectively promotes readout fidelity by reducing noise variances in readout waveforms. Its modulated nature encourages adaptable scalability for the circuit topology under detection and its linear-correlation nature permits time-domain measurements at desired time step and duration. The proposed TRMNN showcases its advantages not only in effectively classifying states into both the ground and excited states but also in achieving a high level of accuracy in reading arbitrary superposition states. Our

experimental results have verified the performance gain, proving the usefulness of this novel architecture. Moreover, the proposed modular network architecture ensures straightforward scalability to handle potential expansions in the size of qubits. It expands the scope of machine learning within the field of research of superconducting qubits and quantum computation in general.

ACKNOWLEDGMENTS

H. I. thanks the support of FDCT of Macau under grants 0015/2021/AGJ and 006/2022/ALC. Y. Z.

thanks the support of NSFC of China under grant 12174178 and the Science, Technology and Innovation Commission of Shenzhen Municipality under grant KQTD20210811090049034.

-
- [1] G. Montavon, M. Rupp, V. Gobre, A. Vazquez-Mayagoitia, K. Hansen, A. Tkatchenko, K.-R. Müller, and O. Anatole von Lilienfeld, *New J. Phys.* **15**, 095003 (2013).
- [2] E. S. Tiunov, V. V. Tiunova, A. E. Ulanov, A. I. Lvovsky, and A. K. Fedorov, *Optica* **7**, 448 (2020).
- [3] S. Ahmed, C. S. Muñoz, F. Nori, and A. F. Kockum, *Phys. Rev. Lett.* **127**, 140502 (2021).
- [4] A. Seif, K. A. Landsman, N. M. Linke, C. Figgatt, C. Monroe, and M. Hafezi, *J. Phys. B: At., Mol. Opt. Phys.* **51**, 174006 (2018).
- [5] Z.-H. Ding, J.-M. Cui, Y.-F. Huang, C.-F. Li, T. Tu, and G.-C. Guo, *Phys. Rev. Appl.* **12**, 014038 (2019).
- [6] I. Convy, H. Liao, S. Zhang, S. Patel, W. P. Livingston, H. N. Nguyen, I. Siddiqi, and K. B. Whaley, *New J. Phys.* **24**, 063019 (2022).
- [7] G. Koolstra et al., *Phys. Rev. X* **12**, 031017 (2022).
- [8] S. Cao et al., arXiv preprint arXiv:2402.09532 (2024).
- [9] F. Arute et al., *Nature* **574**, 505 (2019).
- [10] J. Clarke and F. K. Wilhelm, *Nature* **453**, 1031 (2008).
- [11] T. D. Ladd, F. Jelezko, R. Laflamme, Y. Nakamura, C. Monroe, and J. L. O’Brien, *Nature* **464**, 45 (2010).
- [12] Google Quantum AI, *Nature*, **614**, 676–681 (2023).
- [13] F. Borjans, X. Mi, and J. R. Petta, *Phys. Rev. Appl.* **15**, 044052 (2021).
- [14] A. H. Myerson et al., *Phys. Rev. Lett.* **100**, 200502 (2008).
- [15] L. Robledo, L. Childress, H. Bernien, B. Hensen, P. F. Alkemade, and R. Hanson, *Nature* **477**, 574 (2011).
- [16] J. M. Gambetta, J. M. Chow, and M. Steffen, *Npj Quantum Inf.* **3**, 2 (2017).
- [17] A. Lupascu, S. Saito, T. Picot, P. C. de Groot, C. J. P. M. Harmans, and J. E. Mooij, *Nat. Phys.* **3**, 119 (2007).
- [18] I. Siddiqi, R. Vijay, M. Metcalfe, E. Boaknin, L. Frunzio, R. J. Schoelkopf, and M. H. Devoret, *Phys. Rev. B* **73**, 054510 (2006).
- [19] Y. Wang, Z. You, and H. Ian, *AVS Quantum Sci.* **5** (2023).
- [20] P. V. Klimov et al., *Phys. Rev. Lett.* **121**, 090502 (2018).
- [21] J. M. Martinis, S. Nam, J. Aumentado, K. M. Lang, and C. Urbina, *Phys. Rev. B* **67**, 094510 (2003).
- [22] V. Tripathi, H. Chen, M. Khezri, K.-W. Yip, E. M. Levenson-Falk, and D. A. Lidar, *Phys. Rev. Appl.* **18**, 024068 (2022).
- [23] P. Mundada, G. Zhang, T. Hazard, and A. Houck, *Phys. Rev. Appl.* **12**, 054023 (2019).
- [24] D. Pitsun et al., *Phys. Rev. Appl.* **14**, 054059 (2020).
- [25] T. Walter et al., *Phys. Rev. Appl.* **7**, 054020 (2017).
- [26] J. Heisoo, et al., *Phys. Rev. Appl.* **10**, 03404 (2018).
- [27] M. Boissonneault, J. M. Gambetta, and A. Blais, *Phys. Rev. Lett.* **105**, 100504 (2010).
- [28] K. Hornik, *Neural Netw.* **4**, 251 (1991).
- [29] G. Cybenko, *Math. Control. Signals, Syst.* **2**, 303 (1989).
- [30] P. Duan, Z.-F. Chen, Q. Zhou, W.-C. Kong, H.-F. Zhang, and G.-P. Guo, *Phys. Rev. Appl.* **16**, 024063 (2021).
- [31] B. Lienhard et al., *Phys. Rev. Appl.* **17**, 014024 (2022).
- [32] E. Magesan, J. M. Gambetta, A. D. Córcoles, and J. M. Chow, *Phys. Rev. Lett.* **114**, 200501 (2015).
- [33] R. Barends et al., *Phys. Rev. Lett.* **111**, 080502 (2013).
- [34] A. Blais, R.-S. Huang, A. Wallraff, S. M. Girvin, and R. J. Schoelkopf, *Phys. Rev. A* **69**, 062320 (2004).
- [35] L. Badri, *Int. Arab J. Inf. Technol.* **7**, 289 (2010).
- [36] Z. Xiao-Ping, *IEEE trans. neural netw.* **12**, 567 (2001).
- [37] J. Heinsoo et al., *Phys. Rev. Appl.* **10**, 034040 (2018).
- [38] J. P. Barrett, *Am. Stat.* **28**, 19 (1974).
- [39] D. Svozil, V. Kvasnicka, and J. Pospichal, *Chemom. Intell. Lab. Syst.* **39**, 43 (1997).
- [40] M. Schuster and K. K. Paliwal, *IEEE Trans. Signal Process.* **45**, 2673 (1997).
- [41] J. Schmidt-Hieber, *Ann. Stat.* **48**, 1875 (2020).
- [42] C. Imrie, S. Durucan, and A. Korre, *J. Hydrol.* **233**, 138 (2000).
- [43] M. Jiang, Y. Liang, X. Feng, X. Fan, Z. Pei, Y. Xue, and R. Guan, *Neural. Comput. Appl.* **29**, 61 (2018).
- [44] D. P. Kingma and J. Ba, arXiv preprint arXiv:1412.6980 (2014).

IV. APPENDIX

A. Network architecture

Neural networks can be classified into various architectural categories, including feedforward neural networks (FNN) [39] and recurrent neural networks (RNN) [40], based on the structure of layers and the connections between neurons. Previous research has demonstrated that the fully connected FNN architecture improves readout

fidelity as a state discriminator for multiple qubits [31]. The architecture of an FNN discriminator is illustrated in Fig. 1(a), where a single neural network is implemented to discriminate between the ground and excited states for all measured qubits. Hence, along with the number of qubits, the network complexity (both the number of hidden layers and the necessary size of training sets) scales up, challenging both readout accuracy and scalability simultaneously.

In contrast, the TRMNN is a network cluster comprising as many FNNs and output function instances as the number of qubits: each qubit matches with a network module with identical internal architecture, as illustrated in Fig. 1(b). Each module includes an input layer, an output layer, and three hidden layers consisting of 900, 250, and 50 neurons, respectively, in between. Intra-layer connections are furnished by rectified linear unit (ReLU) [41] for activation, whereas the output layer is connected to a linear output activation function often used in regression prediction [42] for probability estimation. State tomography for qubits here is akin to linear regression analysis: the neural network takes a sampled waveform as the input to generate in an output neuron a score over the interval $[0, 1]$ based on its similarity or distance to the preset ground or excited state waveforms defined as 0 and 1, respectively.

FNN equipped with a discriminator incorporates a softmax function in the output layer, which is a non-linear output activation function widely used for classification problems [43]. It acts as a binary classifier in enhancing distinguishability between ground and excited state waveforms but has the drawback of misclassification when the qubit superposition is close to but not identical to either the ground or the excited state. TRMNN, on the other hand, generates a direct output linearly correlated with the population inversion without additional enhancement, thereby enhancing the readout fidelity for all superposition states. The trained network focuses on mitigating the noise effect rather than improving binary distinguishability. Moreover, the fixed architecture from the input layer to the output function of each module permits straightforward scalability by expanding the module number when the number of qubits is increased. Through parallel computational expansion, the increase in the number of network modules has a modest impact on computational resources.

B. Dataset preparation and network training

TRMNN requires training through supervised learning before it can effectively operate. The training dataset comprises fixed-length sampled waveforms corresponding to the ground and the excited states of its paired qubit. The experimental results shown below are obtained from

4,000 probe shots each for either the ground or the excited state, where each shot consists of a sequence of 2,000 sampled IQ point pairs in one microsecond.

System parameters	
Xmon qubit frequency	3.842 GHz
Readout resonator frequency	5.331 GHz
Coupling strength	85 MHz
Readout resonator linewidth	1.1 MHz
T_1	26 μ s
T_2	5 μ s

Table III. The parameters in the testing system of a single xmon qubit coupled to a readout resonator.

During network training, the qubit is initially prepared according to the target state expected. To be exact, as illustrated in Fig. 2, the computer issues commands to the AWG such that it either sends a π -pulse to invert the qubit or remains silent to let the qubit stay at the ground state. Simultaneously, tagging information of the corresponding state is transmitted to the TRMNN to associate each emitted waveform sampled on the ADC with each tag.

The connection weights between the neurons are adjusted by minimizing the error in the output compared to the expected result. To optimize training performance, a validation-training set ratio of 0.2 is employed, utilizing the Adam optimizer [44] with mean squared error as the loss function. Then, the trained TRMNN inherently distills waveform differences in the tagged training set and averages out the random noise in the connection weights. Consequently, the output neuron accumulates a weight proportional to the similarity score where the noise has been filtered out during the accumulation. When this weight is read through the output linear activation function, its variance and fidelity would be improved over the pre-network raw readout.

After the training is completed, TRMNN receives the testing waveform of an arbitrary superposition state, which can consist either of a single shot or a set of repetitive measurements. By comparing it to the trained waveforms, the neural network generates a similarity score and translates it into a qubit population. In the case of repetitive measurements, TRMNN directly produces an averaged result and variance for the testing set, removing the averaging step necessary for raw IQ quadratures readout.

The time resolution of TRMNN is accomplished by associating the testing waveform with the qubit control pulse length. Particularly, the readout results can be plotted against arbitrary driving pulse lengths, enabling comprehensive time-domain state tomography over desired durations. Therefore, it can capture Rabi oscillations at specific time steps, bypassing the limitation of discriminator-type networks.